JOURNAL OF MATERIALS SCIENCE 31 (1996) 3921–3927

Direct observations and comparison of crater cross-section microstructures in copper targets for aluminium projectiles impacting at 1.4 and 6.7 km s^{-1}

S. A. QUINONES, J. M. RIVAS, E. P. GARCIA, L. E. MURR
Department of Metallurgical and Materials Engineering, The University of Texas at El Paso, El Paso, TX 79968 USA

Light and transmission electron microscopy observations of impact crater-related microstructures in copper targets have revealed dramatic differences in the extent and type of microstructures. For a crater formed by a 6.4 mm diameter aluminium (1 1 0 0) spherical projectile impacting at 1.4 km s^{-1}, a narrow ($\sim$20 μm) recrystallized zone extended axially outward from the crater wall, with dislocation cells which increased in size extending from this zone. By comparison, a crater formed by a 3.2 mm diameter aluminium (1 1 0 0) spherical projectile impacting at 6.7 km s^{-1} exhibited a recrystallization zone extending more than 200 μm axially from the crater wall, a connecting zone of increasingly dense microbands, having an axial width of about 2000 μm. This zone converged upon a region of dislocation cells which increased in size away from the crater wall. These observations highlight important microstructural differences in cratered metal targets in the hypervelocity impact regime in contrast to the lower-velocity regimes where shock-wave and related ultra-high-strain-rate effects are unimportant.

1. Introduction

Since the beginning of Earth-orbiting phenomena characterized by Sputnik, impact damage in its broadest sense has been of major concern [1]. For space craft in low Earth orbit (LEO) at around 500 km from the Earth's surface the average speed is about 7.7 km s^{-1}. However, because LEO is becoming increasingly populated with a wide spectrum of debris and other bodies, in complex orbital systems, collisions are possible with impact speeds between 0–80 km s^{-1}; including the effects of velocity vector summation for micrometeoroids in orbit around the Sun which can intercept the LEO environment. Fortunately, few collisions occur at the highest speeds, and the average impact velocity seems to be around 19 km s^{-1} [2]. Co-orbiting and counter-orbiting impacts occurring in the leading or trailing surfaces of spacecraft or orbiting platforms have speeds between about 2–20 km s^{-1} [3,4], and roughly 30 to 40 per cent of these impacts now appear to be attributed to man-made debris particles [4,5]. The impact speeds are independent of particle sizes and masses.

To understand impact phenomena, particularly impact craters, laboratory simulations have been conducted for roughly 40 years. Unfortunately, existing experimental facilities cannot sensibly replicate speeds above about 8 km s^{-1}, which limits the examination of crater depth/diameter ratios (p/D_c), which have come to be considered constant ($D_c \cong 2p$) by many investigators, especially in the hypervelocity range (> 5 km s^{-1}) [6]. While it is possible to use crater morphology or geometry to differentiate between low encounter velocities (< 2 km s^{-1}) and hypervelocity events > 5 km s^{-1}, there is no systematic variation of crater rim height, width, or ratios of these parameters normalized by crater diameter, D_c, for example, which can be related to particle velocities in excess of about 5 km s^{-1} [7].

The examination of a wide range of impact craters found on a variety of metal surfaces of the NASA-long duration exposure facility (LDEF) after 69 months in LEO showed an estimated impact crater population of more than a billion [8]. To assist in the interpretation of these crater populations, especially in aluminium alloy targets in space-exposed surfaces from LDEF, Bernhard and Hörz [9] recently conducted laboratory simulations of cosmic-dust impacts into aluminium 1100 (annealed) targets with 3.2 mm soda-lime glass projectiles travelling at velocities between 0.7–7 km s^{-1}. They found p/D_c values ranging from > 0.5 to < 0.8. More importantly, they observed a peak of $p/D_c \cong 0.8$ near 2 km s^{-1} which declined at velocities on either side of 2 km s^{-1}, reaching minimum values of $p/D_c \cong 0.58$ between about 4–7 km s^{-1}. It might be expected that the p/D_c ratio in metal targets would decline towards zero at very low impact velocities because in the very low impact velocity range the impact conditions can be considered to

0022–2461

be predominantly elastic. However the rapid rise to a maximum p/D_c value in the velocity (u_0) range $0.4 < u_0 < 4\,km\,s^{-1}$ appears to indicate a dramatic variation in target material behaviour in response to the emergence of impact velocity-dependent deformation ranges. These ranges extend from predominantly elastic (perhaps elasto–plastic) at very low impact velocities to shock–plastic in the hypervelocity range.

Over the past three decades, dozens of models to calculate p/D_c for projectiles of a density ρ_p impacting targets of density, ρ_t, at a velocity u_0, have been postulated in the velocity range $3\,k < u_0 < 21\,km\,s^{-1}$ [10]. Some of these models have attempted to consider the impacting particle, whilst others have addressed the target material behaviour and properties (yield strength, hardness, fracture strength, etc.), but there have been no attempts to systematically examine the microstructure associated with impact craters in specific metal targets. In fact, it appears that few if any studies of LEO or LEO-simulated impact craters in metal targets have ever even considered the initial microstructure of the target (grain size, morphology, etc.).

We recently examined a large (0.8 mm diameter) impact crater cross-section microstructure on a stainless steel bolt from LDEF utilizing transmission electron microscopy (TEM) [11]. Deformation twins were observed at distances approximately 1 crater diameter ($\sim D_c$) below the crater wall. This led to the conclusion that a strong shock wave (or high shock pressure) was associated with the crater formation because such deformation twins have been previously associated with plane-wave shock deformation of stainless steels [12]. The critical twinning pressure for stainless steel has been estimated to be 10 GPa; consequently the minimum shock pressure acting at $\sim D_c$ below the crater wall would be expected to be at least 10 GPa [13]. The unattenuated pressure at the base of the crater may even have been double this pressure. For an interplanetary dust particle (IDP) having a density assumed to be $2.3\,g\,cm^{-3}$ this pressure would require a corresponding hypervelocity of $6.4\,km\,s^{-1}$. This velocity was calculated by applying the Bernoulli equation: $P_B = 0.5\,\rho^* u_0^2$; where $\rho^* = \rho_p\rho_t/(\rho_p^{1/2} + \rho_t^{1/2})^2$, and P_B is the peak shock pressure in GPa (~ 20 GPa), ($u_0 = 2P^{1/2}/\rho^*$).

It should also be noted that the Bernoulli equation is strictly only applicable to fluids, therefore its extension to solid-state crater formation is an approximation. The actual shock pressure associated with the initial impact at the target surface is determined by the general Hugoniot relations: $P_s - P_0 = \rho\, u_p U_s$ where P_0 is the pressure in the target, ahead of the shock front (and is assumed to be zero), while u_p and U_s are the corresponding particle and shock velocities respectively. Considering the density differences to be accommodated in the concept of acoustic impedances, the instantaneous, peak shock pressure at impact (and along the impact axis) is given by $P_s = Z_p Z_t u_0/(Z_p + Z_t)$ where the corresponding impacting particle (p) and target (t) impedances are defined by $Z = \rho(C_0 + Su_p) \times u_p$, where ρ is correspondingly ρ_p or ρ_t, C_0 is the bulk sound velocity in the target material and S is target material specific and related to the Gruneisen parameter. Solutions for the Hugoniot shock pressure equations are outlined in Meyers [14], and are observed to be many times the calculated Bernoulli pressure ($P_s \gg P_B$). However, the attenuation of this shock wave along the impact axis during crater formation is certainly complex and often rapid. In general the wave decays with the inverse of distance from the impact point. Calculating P_s for the case in point results in a peak pressure of 250 GPa, which is of course well above the plane-wave shock twinning pressure for stainless steel.

In this preliminary study, we have compared the residual microstructures and microhardness profiles in cross-sections for laboratory-produced impact craters in oxygen free high conductivity (OFHC) copper targets at two extreme impact velocities: $1.4\,km\,s^{-1}$ and $6.7\,km\,s^{-1}$. We chose copper because it has a critical (plane-wave shock) twinning pressure of ~ 20 GPa, estimated to be half that for aluminium 1100 [13], which means that we were capable of producing the necessary twinning pressures using aluminium 1100 projectiles at the upper limit of our laboratory gun impact velocities ($\sim 7\,km\,s^{-1}$). In addition, the deformation behaviour of copper has been studied extensively over a wide range of strains and strain rates. These have included surface erosion (where elastic theory was invoked [15, 17]), and shock [12] and high-strain-rate deformation associated with copper shaped charges [18, 19].

2. Experimental details

The experiments in this study utilized 3.2 and 6.4 mm diameter 1100 aluminium projectiles impacting 1.3 cm thick OFHC copper rolled-plate targets having as-fabricated grain sizes ranging from 30–40 μm. A $1.4\,km\,s^{-1}$ velocity projectile was obtained via a 7 mm powder-propellant gun, while a 5 mm light-gas gun was utilized to achieve a projectile velocity of $6.7\,km\,s^{-1}$. These two experiments produced two craters, shown in cross-section in Fig. 1, with dimensional measurements related to the initial target surface plane which was used as a reference point as follows: $u_0 = 1.4\,km\,s^{-1}$ ($D_c = 11.5$ mm; $p = 4$ mm; $p/D_c = 0.35$); $u_0 = 6.7\,km\,s^{-1}$ ($D_c = 11.0$ mm; $p = 5.5$ mm; $p/D_c = 0.5$). The hypervelocity impact sample ($u_0 = 6.7\,km\,s^{-1}$) also produced a regular spall which is not shown in Fig. 1.

Each crater was cut in half, revealing the cross-sections shown in Fig. 1. These cross-sections were polished and etched to reveal the grain structure using a final polish involving 0.3 μm alumina followed by a solution etch composed of 100 mL of water, 4 ml of saturated sodium chloride solution, 2 g of potassium dichromate and 8 mL of sulphuric acid at a temperature of 0 °C. These etched cross-sections were observed in an optical metallograph at a magnification of 500x.

Digital, automated Vickers microhardness measurements were made on the polished and etched crater half-sections utilizing a 50 g–f load. Measurements were made as close to the crater wall as possible and extended along a central axis representing normal particle impact from the crater base.

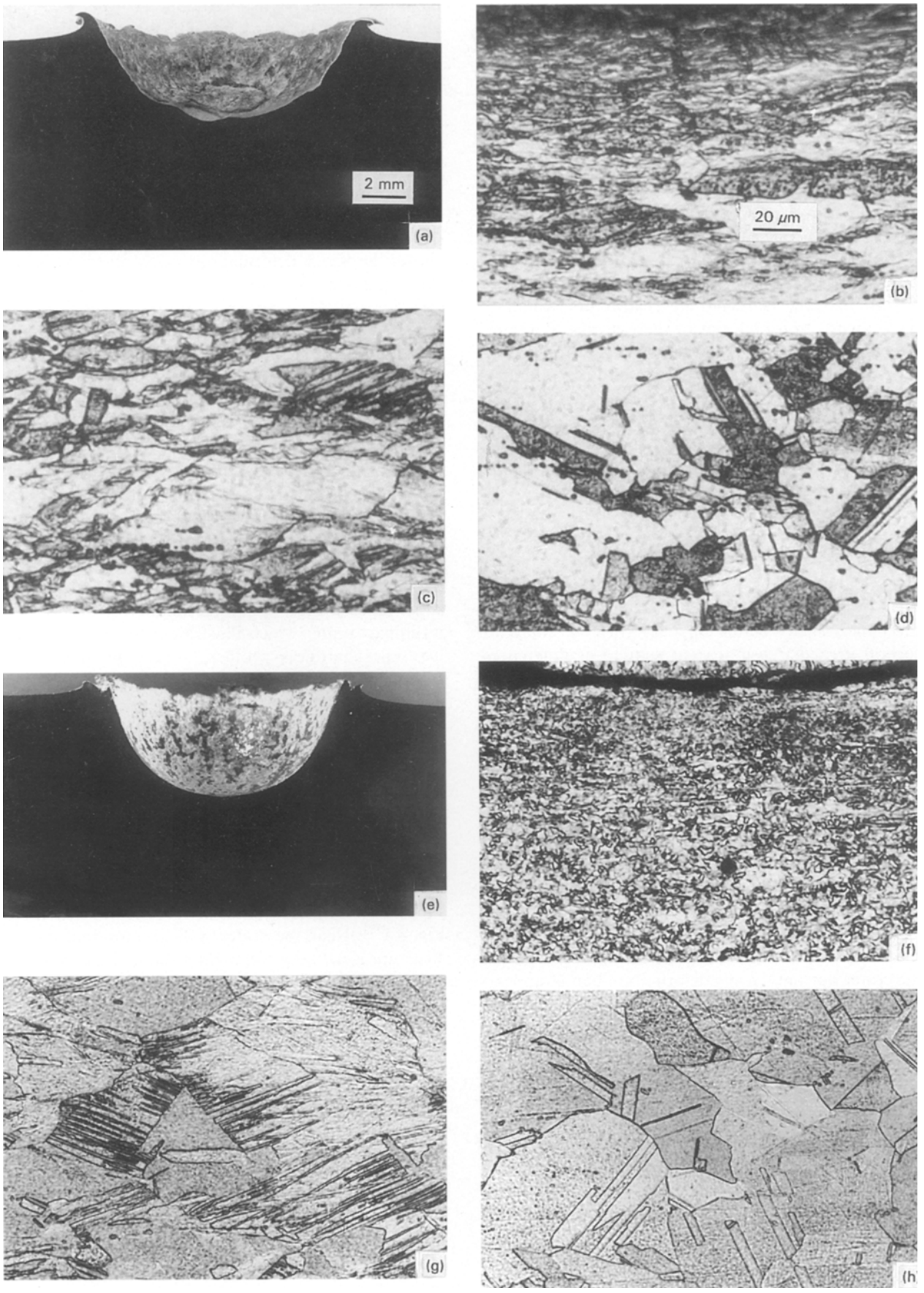

Figure 1 Comparison of prominent microstructural features for low (1.4 km s^{-1}) and hypervelocity (6.7 km s^{-1}) impact craters in OFHC copper targets observed by light microscopy of polished and etched cross-sections along the impact axis. Low-velocity crater to the left (a) exhibits plastic flow extending from the crater wall (b) and (c). (b) Extends from the crater bottom and (c) is located roughly 0.5 mm from the crater wall. (d) Shows the undeformed target grain structure. The average grain size is 37 μm. Hypervelocity crater to the left (e) exhibits a narrow recrystallization zone extending from the crater wall (f) which merges with a plastic deformation/grain distorted zone, followed by a zone exhibiting dense deformation bands (g) in otherwise undistorted grains. (h) Shows the undeformed target grain structure. The average grain size is 31 μm. The microband zone shown in (g) is located roughly 1.2 mm from the crater wall. The size bars in the light microscope images (b) to (d) and (f) to (h) are the same as shown in (b). The size bar of (e) is shown in (a).

Specimens for TEM were prepared by taking two thin slices from the matching crater half-section having a thickness of roughly 0.2 mm. Three mm diameter discs were punched from these slices at specific locations relative to the crater wall, polished, dimpled, and electropolished at 8 volts and 15 °C in a Tenupol 3-jet polisher using a solution of 825 mL of distilled water, 300 mL of phosphoric acid, 375 mL of ethanol, 75 mL of propanol and 7.5 g of urea. In addition, thin slices were made in the matching crater half-section at oblique angles to the plane of the section, and next to the crater wall, in order to allow thin discs to be punched adjacent to the crater wall. To ensure that the observed microstructure would be within a fraction of 1 mm of the crater wall, the exposed crater bottom was coated with a stop-off lacquer until the opposite surface was electropolished up to the wall surface. The electron transparent thin disc specimens which resulted were observed in a Hitachi H-8000 analytical transmission electron microscope operated at a 200 kV accelerating potential in the conventional TEM mode.

3. Results and observations

Fig. 1 shows the significant, comparative microstructures for the low velocity crater ($u_0 = 1.4\ km\,s^{-1}$) and the hypervelocity crater ($u_0 = 6.7\ km\,s^{-1}$). There are several immediately apparent significant differences. The low velocity crater (Fig. 1(b–d)) exhibits a regular transition from heavy plastic deformation (and grain distortion) at the crater wall to the relatively undeformed and undistorted grain structure characteristic of the original target plate. This occurs at a distance of roughly 2.2 mm along the impact axis, measured from the crater bottom. In contrast, the hypervelocity crater (Fig. 1(f–h)) exhibits a narrow zone next to the crater bottom characteristic of dynamic recovery and recrystallization. This extends roughly 0.2 mm from the crater wall, and shows a transition to a heavily plastically deformed (grain distorted) region which extends roughly 1 mm along the impact axis, measured from the crater bottom. Heavy deformation bands, appearing to be coincident with the {1 1 1} annealing twin boundary traces, are observed to begin in this plastically deformed zone, and to extend more than 2.2 mm from the crater bottom, well into relatively undistorted grains. The corresponding and associated geometrical parameters and pressures for these two impact craters are listed for comparison in Table 1.

These microstructural features are corroborated and clarified by comparing the corresponding TEM bright-field images for the two different crater regimes illustrated in the light microscope views of Fig. 1, as shown in Fig. 2. Consistent with the microstructural evolution for the low-velocity crater in Fig. 1(b–d) the TEM observations shown in Fig. 2(a–c) show dislocation cells whose sizes increase systematically with distance from the crater bottom with some recrystallization very close to the crater wall (Fig. 2a). Fig. 2d illustrates the unambiguous, recrystallized grain structure extending from the hypervelocity crater wall, where growth and annealing twins are also absent as a consequence of the recrystallization process. Fig. 2e shows the heavy deformation bands observed below the hypervelocity crater wall (Fig. 1g) to be microbands essentially coincident with the traces of {1 1 1} planes, but lacking any deformation twin character. Fig. 2e also shows the dislocation density in the microband region of the hypervelocity crater to be as high as that in the heavy plastically deformed region directly under the low-velocity crater wall (compare Fig. 2(a and e)).

The distinct differences in the residual deformation phenomena associated with the two impact craters in the copper targets implicit in both Figs 1 and 2 are also confirmed by comparing the corresponding microhardness profiles as illustrated in Fig. 3. The microhardness data for the two impact craters are superimposed on a computer-simulated, hypervelocity impact crater which illustrates, in contrast to the two microhardness profiles, a very limited, linear strain profile based strictly on the computer-generated deformation behaviour. In effect, the low-velocity impact crater microhardness curve shown plotted in Fig. 3 essentially follows this simple deformation behaviour along the impact axis, and is consistent with the simple dislocation cell size evolution away from the crater wall illustrated in Fig. 2. The microhardness profile for the hypervelocity impact crater (right profile in Fig. 3) in copper is very different from the low-velocity impact crater (left profile in Fig. 3), and supports the microstructural features illustrated in Fig. 2(d–f). Near the crater wall, the residual microstructure is actually softer than the original, starting target plate, becoming increasingly harder, and reaching a maximum, in the region characterized by residual deformation microbands. The hardness profile extends well away from the crater bottom for the experimental impact craters in sharp contrast to the very limited extension for the computed crater in Fig. 3.

4. Discussion and conclusions

This study establishes the unique microstructural features associated with low-velocity impact crater

TABLE I Experimental crater parameters

Impact velocity u_0 ($km\,s^{-1}$)	Impact particle (1100Al)		Target density, ρ_t ($g\,cm^{-3}$)	Instantaneous shock pressure P_s (GPa)	Bernoulli pressure P_B (GPa)	p cm	D_c (cm)	p/D_c
	diameter, d_p (cm)	ρ_p ($g\,cm^{-3}$)						
1.4	0.64	2.70	8.96	18	1.1	0.40	1.15	0.35
6.7	0.32	2.70	8.96	140	25.4	0.55	1.10	0.50

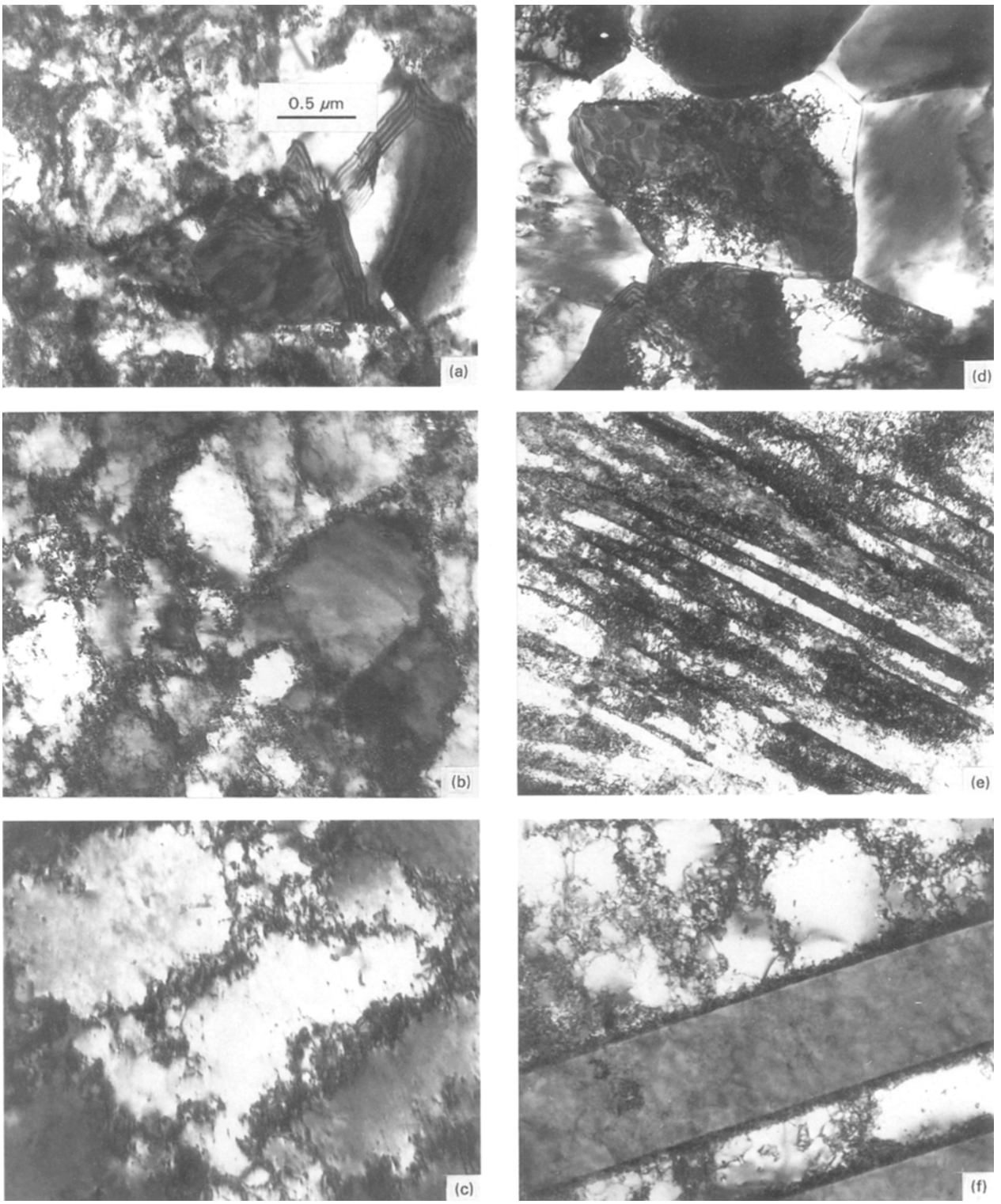

Figure 2 TEM bright-field images corresponding to the impact crater-related microstructural evolution illustrated in Fig. 1. Images to the left (a), (b) and (c) correspond roughly to zones shown in Fig. 1(b–d) and show dense dislocations, recrystallized grains, and small dislocation cells which increase in size and grow commensurate with the target dislocation structure shown in (c). Images to the right (d and e) show corresponding, prominent microstructural features associated with the microstructural zones shown in Fig. 1(f–h) respectively. (d) Shows fine, recrystallized grains devoid of twin boundaries. (e) Illustrates prominent microbands and very high dislocation density. The grain surface orientation in (e) is (112) and the microbands are nearly coincident with the $[1\bar{1}0]$ direction. The microband interfaces exhibit misorientations of roughly 2°–4° while the average microband width is around 0.1 μm. (f) Shows the target microstructure to consist of some large dislocation cells as a result of plate fabrication as in (c). Magnification for all TEM images are the same as shown in (a).

formation in contrast to hypervelocity impact crater microstructures. Low-velocity impact craters ($< 2\ \mathrm{km\,s^{-1}}$) in copper targets can be considered to be characterized by elastic–plastic deformation associated with heavy deformation (high stresses or strains) near the crater wall, which fall off with distances away from the crater wall. They correspond roughly to reciprocal dislocation cell sizes (1/d) in much the same way that very low velocity erosion craters ($u_0 < 0.1\ \mathrm{km\,s^{-1}}$) are characterized: $1/\mathrm{d} \propto u_0^{2/5}$ [16]. Indeed, the maximum, normal contact pressure associated with a classically elastic indentation crater

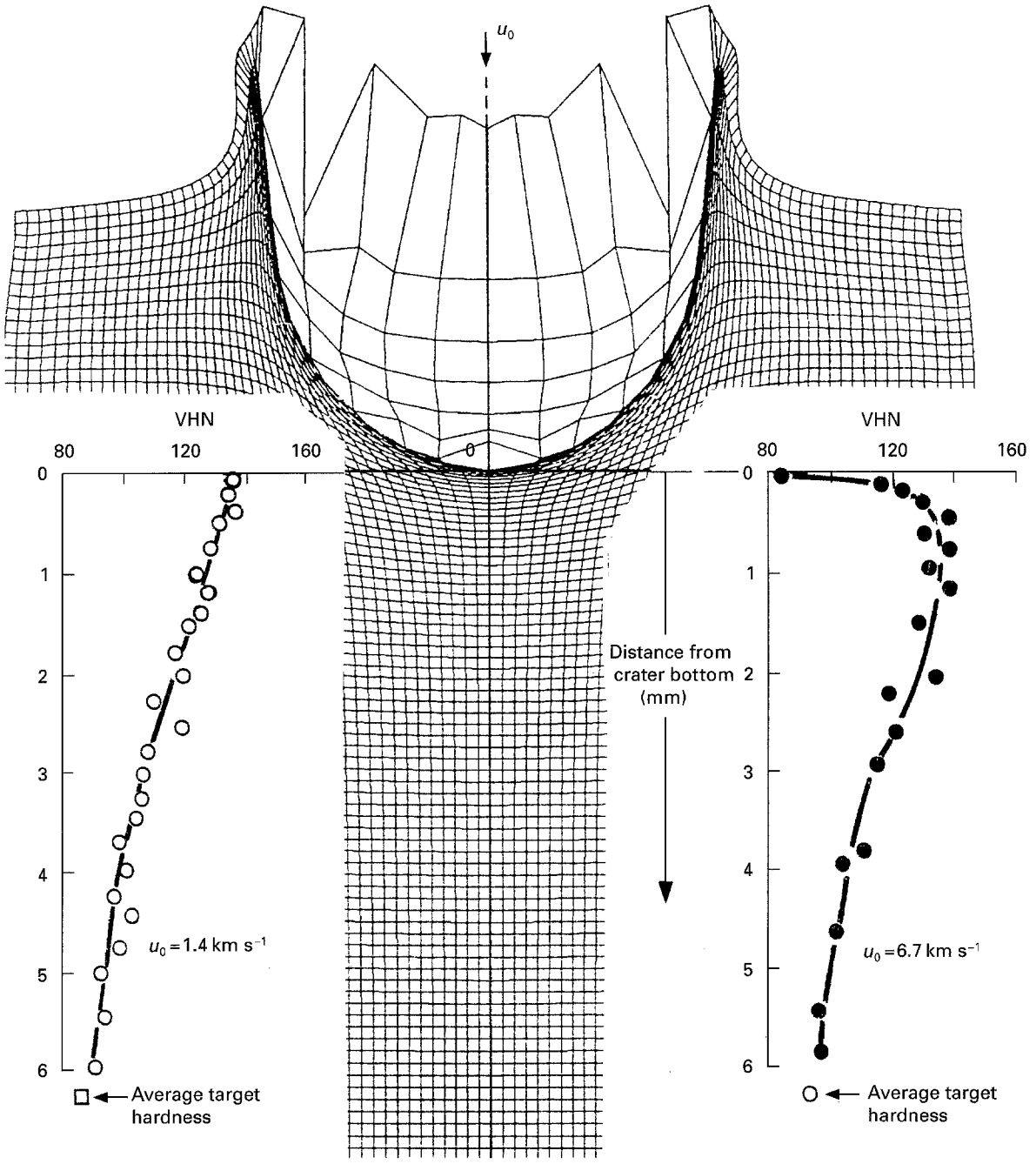

Figure 3 Comparison of low-velocity (left) and hypervelocity (right) impact crater-related microhardness profiles along the normal impact axis, below the crater bottoms. This microhardness data is shown in coincidence with a computer-simulated hypervelocity impact crater (for $u_0 = 13\ \mathrm{km\,s^{-1}}$). Note the crater-related, finite element deformation (strain) features which emanate outward from the crater wall. The computed crater size and related dimensional scale corresponds to the microhardness data (in mm) and allows the simulated image features (corresponding linear strains) to be qualitatively compared with the microhardness profiles.

is often given by $P = \pi^{-1}(2.5\pi\rho_p)^{1/5}(E_p/(1-v_t))^{4/5} \times u_0^{2/5}$, where E_p and v_t are the particle elastic (Young's) modulus and Poisson's ratio for the target, respectively [20]. This pressure dependence is in contrast to the high velocity and hypervelocity regime where the Bernoulli equation is applied: $P_B = 0.5\ \rho^* u_0^2$ (or in comparison with the pressure relationship noted above: $P_B = 0.5\ \rho^* u_0^{10/5}$). However, the differences between the velocity regimes $< 2\ \mathrm{km\,s^{-1}}$ and $> 6\ \mathrm{km\,s^{-1}}$ compared in this study are most prominently illustrated by the extent of recrystallization near the crater wall. This is a prominent residual microstructural feature for the hypervelocity crater in OFHC copper, extending roughly 200 μm axially (along the impact axis, u_0, shown in Fig. 3) from the crater wall as compared to an extremely narrow zone extending only about 20 μm axially from the crater wall for the low-velocity crater (Fig. 1b). In addition, there is a distinct zone of high residual hardness and associated deformation microstructures, somewhat removed from the crater wall for the hypervelocity crater (Fig. 1g), which is assumed to be the result of shock-related phenomena. This zone does not appear in the low velocity crater microstructure, and only a few deformation microband features are noted in Fig. 1c for example.

Similar observations of a narrow zone of recrystallization near the crater wall have also been observed in single-crystal and polycrystal iron targets where craters (~1 mm diameter) were created by high-pressure

laser pulses [21]. In this related crater work, a (presumed) deformation-induced twin zone extended outward from the recrystallized zone, with the recrystallized and twinned zone widths increasing with increasing peak shock pressure [21]. Microhardness profiles for iron craters [21] exhibited a shape very similar to that illustrated in Fig. 3 for the hypervelocity impact crater in copper.

In contrast to craters in aluminium 1100 targets recently examined by Bernhard and Hörz [9] for 3.2 mm diameter soda-lime projectiles (ρ_p = 2.2 g cm^{-3}), the corresponding ratio of 0.8 at the peak of the p/D_c versus u_0 curve, has a minimum of 0.35 for the copper crater at an impact velocity of 1.4 km s^{-1} for a 6.4 mm aluminium 1100 projectile (ρ_p = 2.7 g cm^{-3}). The p/D_c ratio in an aluminium target was roughly 0.55 in contrast to 0.5 for the copper crater at 6.7 km s^{-1} (Table 1). These differences suggest that the corresponding p/D_c versus u_0 curve for copper, in contrast to that for 1100 aluminium, over a range of particle impact velocities ranging from 0.7–7 km s^{-1}, would be very different even for identical impact parameters (particle size, density, and velocity).

It is apparent from Fig. 3 that conventional hydrocode simulations contain no microstructural information in connection with modelling hypervelocity impact craters in metal targets. Thus neither the recrystallization or recovery zones are represented, and there is absolutely no representation of the intense deformation microstructures which are created by the shock wave loading well below the plastic deformation zone, and well below the crater bottom (> 0.2 D_c below the crater bottom). There is only a zone of high strain which is rapidly relaxed with distance from the crater wall.

In order to develop meaningful hydrocode representations of hypervelocity impact crater phenomena in thick metal targets, it will be necessary to very seriously and systematically investigate the residual crater dimensions and associated microstructures for a wide range of impact parameters in numerous metal or alloy targets. Especially important will be the effects of the initial target grain size and dislocation density and microstructures on p/D_c ratios versus u_0, as well as the evolution of residual, crater-related microstructures in the target materials.

More detailed investigations involving different, effective shock pressures (and corresponding hypervelocity impacts) are also necessary to understand the development of microbands illustrated in Fig. 1a and Fig. 2e. While microbands have been observed in many deformed metals, and even shock-loaded copper [22], the mechanism of formation is not well understood, and certainly the lack of deformation twins and preference for microbands even though the requisite peak shock pressure was apparently achieved during crater formation, is not understood. The combined effects of shock, rarefaction, adiabatic heating, and plastic deformation may explain this microstructural occurrence.

Acknowledgements

This research was supported in part by a NASA-Johnson Space Center Grant (NAG-9-481) and a NASA Graduate Research Training Grant (NGT-70343) (S.A.Q.). The work was also supported by the Phelps-Dodge Foundation Scholarship Program (S.A.Q. and E.G.). We are grateful to Dr. Fred Hörz and Ron Bernhard, NASA-Johnson Space Center, who provided archived impact craters for this study, and Dr. Mark Wilkins, Lawrence Livermore Laboratories for providing the computer hydrocode crater simulation in Fig. 3.

References

1. F. L. WHIPPLE, The Meteoric Risk to Space Vehicles Proceedings of the International Astronomical Congress (Springer-Verlag, Wien, 1958) p. 418–428.
2. H. A. ZOOK, Lunar and Planetary Science XXI (Lunar and Planetary Institute, Houston, Texas, 1990) p. 1335.
3. R. PETERSON, Reproduced in F. Hörz *et al.* NASA-Langley Research Centre, CP 3194, (1992) pp. 487–493.
4. D. E. KESSLER, *ibid.*, p. 585.
5. F. HÖRZ, R. P. BERNHARD, J. WARREN, T. H. SEE, D. E. BROWNLEE, M. R. LAURANCE, S. MESSENGER and R. B. PETERSON, Preliminary Analysis of LDEF instrument A0187-1 chemistry of micrometeoroids experiment, in LDEF-69 Months in Space, First Post Retrieval Symposium (held in Kissimmee, Florida, June 2–8, 1991), NASA Conference Publication 3134, Part 1, A. S. Levine (ed), (NASA Langley Research Centre, Hampton, VA, 1991) p. 487.
6. B. G. COUR-PALAIS, *Int. J. Impact Engng.* **5** (1987) 221.
7. L. E. MURR and J. M. RIVAS, *ibid.* **15** (1994) 785.
8. L. E. MURR and W. H. KINARD, *Amer. Scientist* **81** (1993) 152.
9. R. P. BERNHARD and F. HÖRZ, *Int. J. Impact Engng.* **17** (1995) 69.
10. W. P. SCHONBERG and R. A. TAYLOR, NASA Tech. Memorandum NASA TM-100358. Marshall Space Flight Center, January 8, 1989.
11. J. M. RIVAS, L. E. MURR, C.-S. NIOU, A. H. ADVANI and D. J MANUEL, *Scripta Metall. et Materialia* **27** (1992) 919.
12. L. E. MURR, in "Shock Waves and High-Strain-Rate Phenomena in Metals", edited by M. A. Meyers and L. E. Murr, (Plenum Publishing Corp., New York, 1981) p. 607.
13. L. E. MURR and K. P. STAUDHAMMER, in "Shock Waves for Industrial Applications", edited by L. E. Murr (Noyes Publications, Park Ridge, N. J., 1988) pp. 1–59.
14. M. A. MEYERS, "Dynamic Behaviour of Materials" (J. Wiley & Sons, Inc., New York, 1994)
15. D. KUHLMANN-WILSDORF, in "Fundamentals of Friction and Wear of Materials", edited by D. A. Rigney (ASM, Metals Park, Ohio, 1981) pp. 119–127.
16. D. KUHLMANN-WILSDORF and L. K. IVES, *Wear* **85** (1983) 361.
17. D. A. RIGNEY, M. G. S. NAYLOR, R. DIVAKAR and L. K. IVES, *Mater. Sci. Engng.* **81** (1986) 409.
18. L. E. MURR, H. K. SHIH. C.-S. NIOU and L. ZERNOW, *Scripta Metall. et Materialia* **29** (1993) 567.
19. L. E. MURR, C.-S NIOU, J. C. SANCHEZ and L. ZERNOW, *ibid.* **32** (1995) 31.
20. A. E. H. LOVE, "The Mathematical Theory of Elasticity" (Dover Publications, New York, 1927) 138–140.
21. M. HALLOUIN, F. COTTET, J. P. ROMAIN, L. MONTY and M. GERLAND, in "Impact Loading and Dynamic Behaviour of Materials, vol. 2." edited by C. Y. Chien, H.-D. Kunze, and L. W. Meyer (Informationsgesellschaft, Verlag, Germany, 1988) pp. 1051–1056.
22. J. C. HUANG and G. T. GRAY III, *Acta Metall.* **37** (1989) 3335.

Received 28 October
and accepted 15 December 1995